

APPARATUS AND DEMONSTRATION NOTES

Jeffrey S. Dunham, *Editor*

Department of Physics, Middlebury College, Middlebury, Vermont 05753

This department welcomes brief communications reporting new demonstrations, laboratory equipment, techniques, or materials of interest to teachers of physics. Notes on new applications of older apparatus, measurements supplementing data supplied by manufacturers, information which, while not new, is not generally known, procurement information, and news about apparatus under development may be suitable for publication in this section. Neither the *American Journal of Physics* nor the Editors assume responsibility for the correctness of the information presented. Submit materials to Jeffrey S. Dunham, *Editor*.

Fast processes imaging device

S. Kasas

Institut de Biologie Cellulaire et de Morphologie, Université de Lausanne, 9 rue du Bugnon, CH-1005 Lausanne, Switzerland, Ecole Polytechnique Fédérale de Lausanne, CH-1015 Lausanne, Switzerland, and Société Vaudoise d'Astronomie, ch. Des Grandes Roches 8, CH-1004 Lausanne, Switzerland

G. Dumas

Société Vaudoise d'Astronomie, ch. Des Grandes Roches 8, CH-1004 Lausanne, Switzerland

G. Dietler

Institut de Physique de la Matière Condensée, Université de Lausanne, CH-1015 Lausanne, Switzerland

(Received 20 March 2002; accepted 26 September 2002)

[DOI: 10.1119/1.1523074]

Taking pictures of processes that occur rapidly is not only fascinating, because of the unusual nature of the images, but can also lead to a better comprehension of physical and biological mechanisms. Unfortunately, high-speed cameras designed to capture these types of events are for the moment too expensive for demonstration purposes.

We recently described in this journal a simple setup using a video camera and a computer to reconstruct the sequence of events occurring after the impact of a projectile into its target.¹ The method consisted of recording several movies of the phenomenon with the video camera and combining their individual images to obtain a time-lapse sequence. This system unfortunately does not permit a synchronization of image acquisition with the fall of the projectile. It therefore leads to variations in the delay between consecutive images composing the time-lapse sequence. To overcome this problem we developed a new apparatus that permits this type of synchronization and which additionally gives better quality images than the previous setup which recorded images with commercial VCR cameras. The new setup consists of a photogate that is connected to a specially designed electronic circuit, two LED panels, and a digital camera. The setup has to be operated in darkness with a wide-open camera. When the projectile crosses the photogate during its approach, it starts a digital timer whose value is compared to a user-defined delay. When the two numbers are equal, the electronic circuit turns on briefly two LED panels and illuminates the scene, which is captured by the camera.

Figure 1 depicts the complete setup. It consists of a 2 m long tube which directs the projectile (in our case a free-

falling marble) towards the target. The tube is followed by a photogate, which informs the electronic circuit of the moment the projectile exits the tubing.

The electronic circuit is basically composed of a timer, four comparators, and six power transistors to switch the LED panels on. It permits the user to select the delay separating the moment the projectile crossed the photogate and the moment the LED panel is turned on. The time delay between the crossing of the light barrier and the first flash can be adjusted to a value between 0 and 99 ms. The circuit can burst up to nine flashes with a programmable duration and a programmable time interval between each flash. The duration of the flash can be adjusted between 0.1 and 9.9 ms. The circuit can also switch the LED panels on for an unlimited duration. This option is used for focusing and for positioning the target and the camera as well. The current delivered during the flash is 400% higher than the nominal value recommended by the LED manufacturer (20 mA) in order to maximize the illumination power of the panels. Since the duration of these pulses is in the range of milliseconds, the life expectancy of the diodes is not affected greatly. The unlimited illumination mode is actually obtained by alternatively turning on and off the panels at a high frequency, which gives the illusion of a constant illumination.

The electronic circuit permits illumination times as short as 100 μ s. (A small modification can permit one to achieve 10 μ s or lower.) To obtain acceptable quality images with such short exposures, one has to illuminate the scene with a bright and responding light source. Light emitting diodes (LED) partially fulfill these requirements: their response times are extremely fast but with a relatively modest illumination power.² To obtain enough light one has to mount sev-

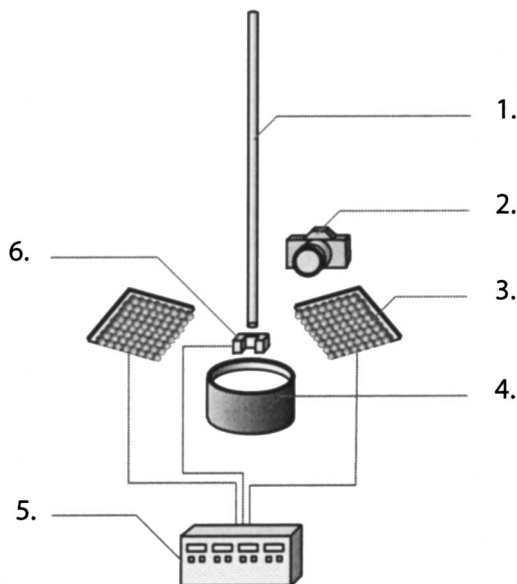


Fig. 1. Schematic drawing of the complete setup: (1) tube, (2) camera, (3) LED panel, (4) target, (5) control electronics, and (6) photogate.

eral dozens of these LEDs on single panels. In our case we use two flat 10×10 cm large panels mounted with 81 LEDs each. The LEDs we are using, called Sloan L5R91H (Distrelec³ catalog number 252216), have a wavelength of maximum emission at 621 nm, a radiating angle of 8° , and a nominal brightness of 8000 mcd. They are among the most powerful LEDs we found on the market.

To optimize the global illumination provided by the panels we first recorded the light emission cone of a single diode and used it to model a one-dimensional strip composed of 9 LEDs. A computer program was written to simulate the illumination of the target with this LED strip; the distance separating each LED was chosen to ensure a homogenous illumination of the target using the results of the simulation. The simulation demonstrated that the best compromise was to keep a panel-target distance of 10 cm with a LED-to-LED distance in the panel of 9 mm.

The images can be captured on any camera; however, we recommend the use of a one, which allows one to display the captured images and to reduce setup adjustments. The only requirement for the camera is a "B" pause option which can last at least 5 s. The images we present in Fig. 2 were captured by a Coolpix 990 Nikon digital camera operated with a 3 s exposure time.

This system is very convenient for capturing images at a precise time after the projectile had crossed the photogate. To obtain a sequence of images, similar to the images obtained

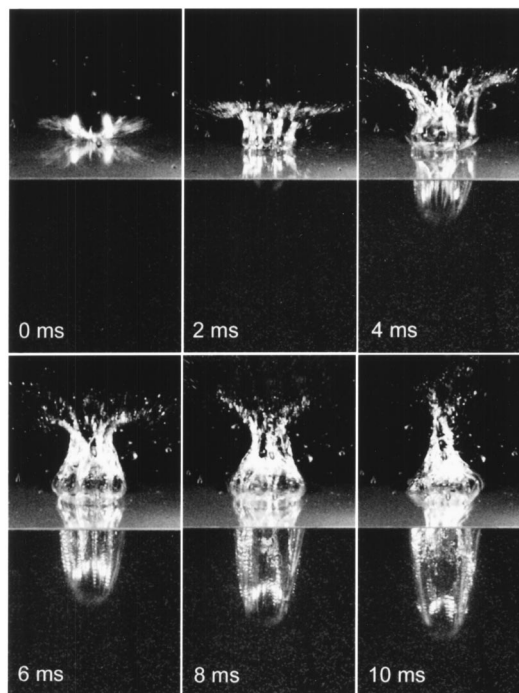


Fig. 2. Time-lapse images of a marble falling into a transparent tank of water with an illumination duration of $500 \mu\text{s}$.

using the previously described setup, one has to repeat the entire experimental process several times, i.e., flattening or exchanging the target, increasing the delay of the first flash, dropping the projectile, and taking a new picture. The multiple flash option permits one to determine, for example, the speed of individual particles being ejected during the impact.

Due to the simplicity of use, the spectacular nature of the images, and the large spectrum of phenomenon it can image, the apparatus will be used in the laboratory exercises for students in physics, forensic sciences, and geophysics.

The authors would like to extend thanks to James DeRose for his help with the preparation of the paper and M. Dominique Breider for providing the facilities for the experiments. This work has been supported by Swiss National Science Foundation grants NB 31-00052587.97 and 2000-065160.01.

¹S. Kasas, G. Dumas, and G. Dietler, "Impact cratering study performed in the laboratory without a fast recording camera," *Am. J. Phys.* **68**, 771–773 (2000).

²N. Holonyak, Jr., "Is the light emitting diode (LED) an ultimate lamp?" *Am. J. Phys.* **68**, 864–866 (2000).

³Distrelec AG, Naenikon, Switzerland, www.murata-europe.com/country/distsw.html

Frustrated total internal reflection: A simple application and demonstration

F. P. Zanella, D. V. Magalhães, M. M. Oliveira, R. F. Bianchi, L. Misoguti, and C. R. Mendonça

Instituto de Física de São Carlos, Universidade de São Paulo, Caixa Postal 369, 13560-970 São Carlos, SP, Brazil

(Received 1 April 2002; accepted 26 September 2002)

[DOI: 10.1119/1.1523075]

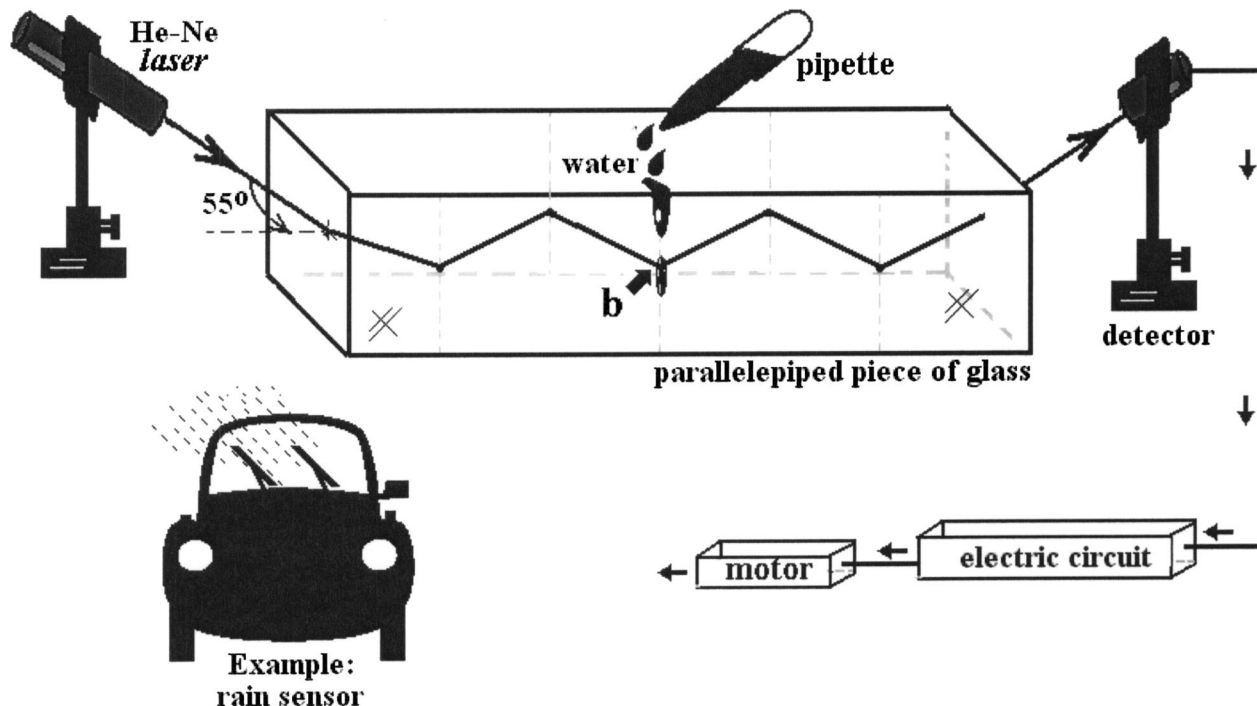


Fig. 1. Diagram of the optical setup.

The total internal reflection process occurs when the internal angle of incidence is equal to or greater than the critical angle.¹ This process is used widely in practical applications, such as the transmission of light through small continuous fibers (optical fibers) and through optical devices which use total reflecting prisms.^{1,2}

When a total internal reflection occurs, the wave amplitude drops exponentially as it penetrates the less dense medium. This exponential decay of the surface wave is frequently called the evanescent wave.³ Imagine that a beam of light traveling within a block of glass is internally reflected at a boundary. Presumably, if you pressed another piece of glass against the first, the air-glass interface could be made to vanish, and the beam would then propagate onward undisturbed. Furthermore, you might expect this transition from total to no reflection to occur gradually as the air film thinned out. In more general terms, if the evanescent wave extends with appreciable amplitude across the rare medium into a nearby region occupied by a higher-index material, energy may flow through the gap in what is known as frustrated total internal reflection (FTIR) or optical barrier penetration.^{1,2} In 1966, Coon described a photon counting experiment to study FTIR which gives very good agreement with the theoretical prediction.⁴ Castro presented a simple experimental arrangement using visible light that allows undergraduate students to perform qualitative experiments of light barrier penetration.⁵

Although applications involving total internal reflection are commonly demonstrated, the same does not occur for the FTIR effect.

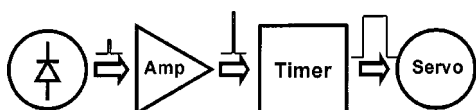


Fig. 2. Block diagram of the electronic system.

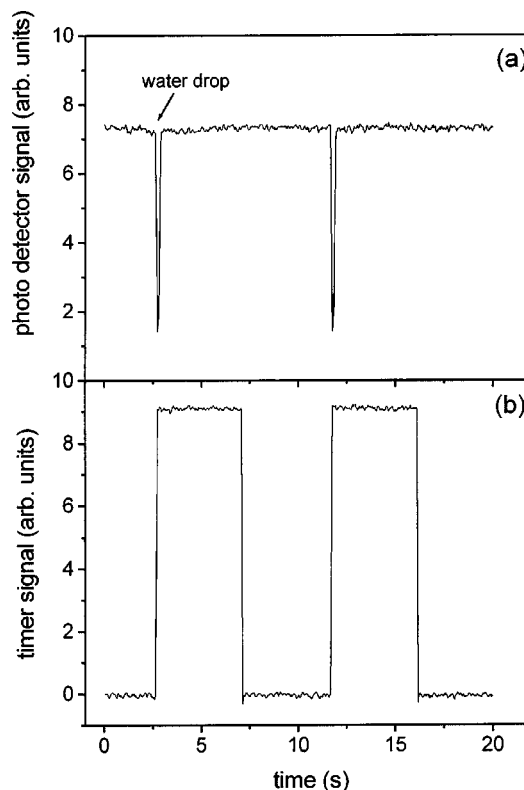


Fig. 3. (a) Time evolution of the laser signal in the photodetector after amplification and (b) monostable signal which commands the servo.

In this note we propose a simple way to provide conditions to the evanescent wave so as to maintain its propagation, thus inducing the FTIR effect. The FTIR effect can occur by perturbing the interface where the total internal reflection occurs. For instance, at a glass–air interface, light suffering total reflection can be perturbed by the presence of a liquid with index of refraction similar to the glass. This idea can be used to perform a remote detection of rain and thus activate a motor. For example, this rain sensor can be used to switch on the windshield wiper blades in a car when the first drop of water is detected. This is the FTIR application demonstration we present here.

Figure 1 shows the experimental setup used. A thick parallelepiped piece of glass ($2 \times 2 \times 10$ cm) was used as a light pipe, in such a way that four total internal reflections occur at the glass–air boundary when the light from a He–Ne laser impinges on the first interface with an angle of $\approx 55^\circ$. The light transmitted from this “pipe” is detected in a common photodiode, generating a DC signal with a 10 mV amplitude. However, when a drop of water slides through the glass at one of the four points on the air interface, the total reflection is frustrated, which decreases the light coming to the detector. In this way, a pulse is generated in the photodetector. This effect is so strong that one can see by eye a decrease in the He–Ne laser intensity at the detector position.

This pulse is then amplified and detected in an electronic circuit which causes a motor to activate. The block diagram for the electronic system we built can be seen in Fig. 2. An operational amplifier (CA3140) was used to convert the diode photocurrent to a voltage signal. The gain was calculated to obtain a level high enough to trigger a timer that keeps the motor working during a selected period of time for each drop. In our case, this time was selected to be around 5 s, which is long enough to dry the windshield in a real car. For timing, a 555-type chip was used in a monostable configuration with suitable external resistance and capacitance values chosen for the servo to be used, in this case a windshield wiper blade motor.

The operation of this demonstration can be seen immediately by dropping water at a point where total internal reflection occurs. For each droplet total internal reflection is temporally frustrated, and motor activation can be seen. Furthermore, an oscilloscope can also be used to check the way this device works. In Figs. 3(a) and 3(b) we present the time evolution of the laser signal in the detector and the monostable (command) signal that drives the servo, respectively. As can be seen in Fig. 3(a), the signal in the photodetector falls for each water droplet that frustrates the total internal reflection.

The graph presented in this figure corresponds to the detector signal after amplification. This change in the photodetector signal enables a timer, which is used to keep the servo working for a determined period of time, approximately 5 seconds in our case. Figure 3(b) shows that for every pulse in the photodetector, the timer signal is enabled, remaining at a high level for 5 s.

This demonstration has proven to be very interesting for undergraduate students of physics and engineering courses because it provides a practical application of a physical phenomenon. Other applications can be elaborated using the same principle, such as, for instance, a liquid level sensor for reservoirs. The equipment used in this demonstration can easily be found in undergraduate teaching laboratories, fulfilling a main goal of this work.

This work was supported by Fundação de Amparo à Pesquisa do Estado de São Paulo (FAPESP). We thank E. Sartori for several helpful discussions.

¹M. V. Klein, *Optics* (Wiley, New York, 1970), Chap. 2.

²E. Hecht, *Optics*, 2nd ed. (Addison-Wesley, Reading, 1974), Chap. 4.

³Sir Isaac Newton, *Optics* (Dover, New York, 1952).

⁴D. D. Coon, “Counting photons in the optical barrier penetration experiment,” *Am. J. Phys.* **34**, 240–243 (1966).

⁵J. C. Castro, “Optical barrier penetration—a simple experimental arrangement,” *Am. J. Phys.* **43**, 107–108 (1975).

A simplified thermoacoustic engine demonstration

Andrej Jeromen^{a)}

Institute of Mathematics, Physics and Mechanics, University of Ljubljana, P.O. Box 2964, SI-1000 Ljubljana, Slovenia

(Received 6 March 2002; accepted 4 October 2002)

[DOI: 10.1119/1.1524163]

Soundwave oscillations in a gas consist of coupled pressure, displacement, and temperature oscillations. Introduction of a solid boundary can change coupling between these oscillations and give rise to a variety of thermoacoustic effects. Among these are thermally driven sound oscillations, the subject of this note.

We have designed and built a simplified thermally driven sound oscillator for didactic demonstration. Our thermoacoustic engine is easy to make and has proved to be an impressive illustration of simplicity, an inherent attribute of thermoacoustic engines. At the same time it is a working demonstration of a heat engine.

In this note, the thermoacoustic engine and the demonstration are described. A basic explanation of the thermoacoustic effect is included. A more thorough introduction to thermoacoustic phenomena can be found in published articles.^{1–3}

A thermoacoustic engine usually consists of an acoustic resonator with an internal structure. In our case, the acoustic resonator is a copper tube closed at one end, and the internal structure is a piece of massive plastic that divides the copper tube into two parts and provides thermal insulation between them, as shown in Fig. 1. On each side, a thin copper disk is pressed onto the plastic by four stainless steel bolts with matching nuts. The plastic part and both copper disks are

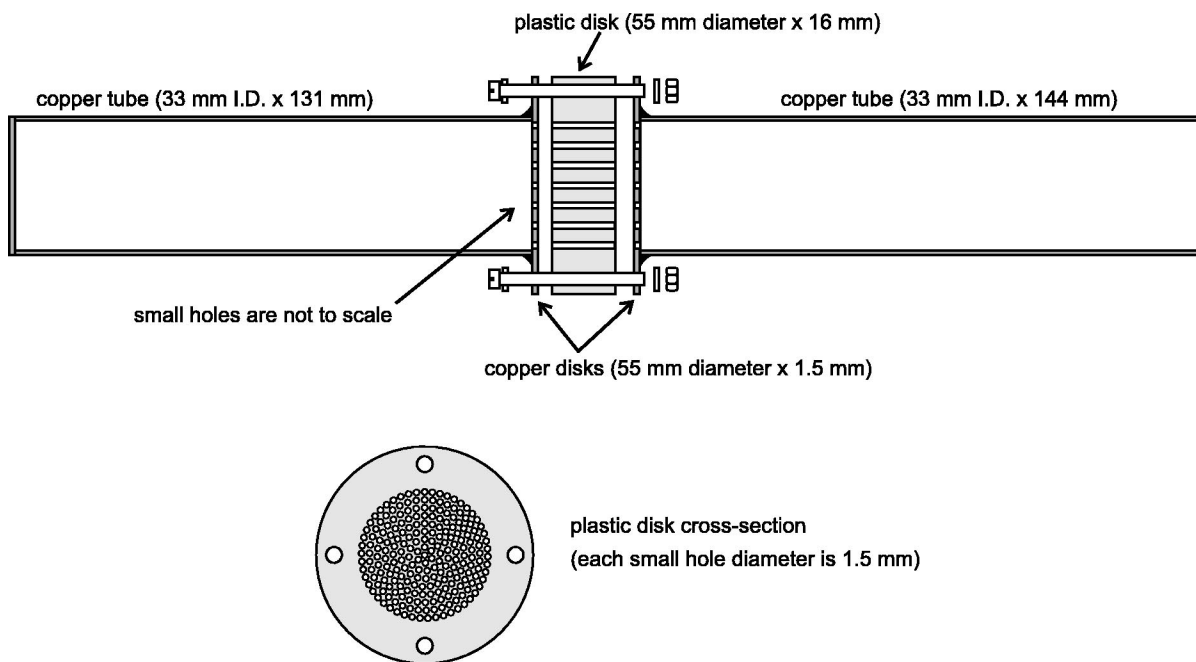


Fig. 1. Drawing of a thermally driven sound oscillator. Each perforated copper disk is soft-soldered to the copper tube. The left copper tube is closed with a soft-soldered copper wall. The engine is assembled using four stainless steel bolts (4 mm diameter \times 25 mm long) with matching nuts. Paper washers were used for better insulation between the two copper parts.

perforated by holes drilled parallel to the resonator axis. The copper disks are soft-soldered on copper tubes and are also used as flanges for assembly of the engine. The engine consists of only three parts: the open and closed copper tubes and the plastic disk.

The engine starts to emit sound when the open end of the tube is cooled and the closed one is kept at room temperature. We dip the open end into liquid nitrogen (77 K) while holding the closed end firmly in the hand to keep it warm (around 300 K). After approximately a minute, a large temperature gradient, parallel to the engine axis, builds up in the plastic part. At the same time, we can feel the onset of oscillations of the gas column in the tube, and in the liquid nitrogen, as the whole engine starts to vibrate. When we withdraw the engine from the liquid nitrogen it starts to emit sound with a frequency of around 200 Hz as shown in the frequency spectrum of Fig. 2. The intensity of the sound is about 60 dB and it can easily be heard throughout a medium-

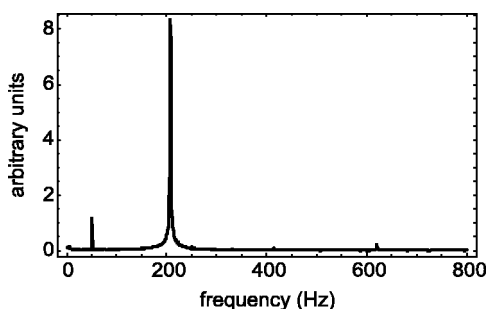


Fig. 2. Frequency spectrum of the emitted sound. It was calculated from a one-second long section of audio recording. The major peak is clearly seen at a frequency slightly above 200 Hz. Small peaks at around 410 Hz and 620 Hz correspond to the second and third harmonic, respectively. The peak at 50 Hz is due to power line interference.

sized lecture hall. The engine sounds for approximately 40 seconds. The frequency of the sound increases as the cold end warms up.

Roughly the same frequency was calculated for a half-closed acoustic pipe of the same length with all its parts at room temperature (length 0.3 m and speed of sound 300 m/s give a fundamental frequency of 250 Hz). Therefore, we can start our short explanation by supposing the air inside the engine oscillates at the fundamental frequency of a half-closed acoustic pipe. The air is compressed while moving towards the closed end (to the left in Fig. 1) and expanded while moving towards the open end of the pipe (to the right

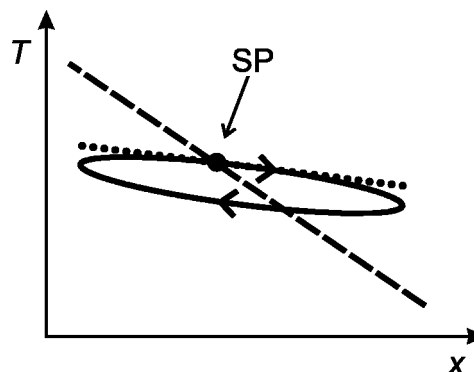


Fig. 3. Qualitative behavior of temperature versus coordinate along the axis of the hole for an oscillating gas parcel. The coordinate x increases towards the open (cold) end of the oscillator. SP denotes the starting point of the thermodynamic cycle description. The dashed line represents the temperature of the plastic wall. The gas parcel delivers heat to the relatively cold wall while it is on the right side and receives heat from the relatively hot wall while it is on the left side. The small temperature variation due to adiabatic compression/expansion of the parcel is shown (with exaggerated slope) as a dotted line.

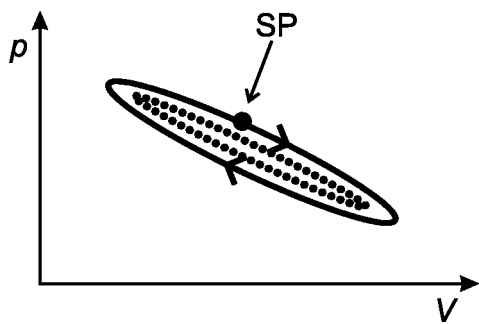


Fig. 4. Qualitative behavior of pressure versus volume for a gas parcel during one cycle. SP denotes the starting point of the thermodynamic cycle description. The parcel is expanded while moving rightwards (in coordinate x), delivering heat to the wall while on the right side, and compressed while moving leftwards, absorbing heat from the wall while on the left side. The directions left/right in the pV diagram correspond to directions of coordinate x in Fig. 3 since the volume of the parcel decreases while the parcel moves left and vice versa. If the temperature gradient in the plastic part were smaller, less heat would be exchanged. Consequently, the thermodynamic cycle would flatten, as shown with the dotted curve.

in Fig. 1). The pressure node and displacement antinode are at the opening of the pipe; the pressure antinode and displacement node are at its closed end.

Let us take a closer look at the temperature of a gas parcel oscillating in a hole bored through the plastic part. A gas parcel is a volume of gas that is small enough to be practically isothermal at all times, yet large enough to enable its macroscopic thermodynamic treatment. Being away from the nodes, the parcel in a hole experiences both displacement and pressure oscillations. When the open end of the resonator is cooled in liquid nitrogen, the temperature gradient in the plastic wall exceeds 120 K/cm. The temperature difference of the plastic wall between the two extreme displacement positions of the parcel is much greater than the temperature difference experienced by the gas parcel due to adiabatic compression and expansion between the same positions. Now, we assume the parcel is in imperfect heat contact with the wall, i.e., a thin layer of gas separates the parcel and the wall. This assumption is very important and we shall return to it later.

In the thermodynamic description it is suitable to start the thermodynamic cycle with the undisplaced parcel having approximately the same temperature as the adjacent wall (starting point labeled SP in Fig. 3). In the vicinity of the parcel's rightmost position (where it is expanded), the parcel delivers some heat to the relatively cold adjacent wall. In the vicinity of its leftmost position (where it is compressed), the parcel receives some heat from the relatively hot adjacent wall. Due to heat exchange with the wall, the parcel is heated and expanded at high pressure. At low pressure it is cooled and contracted.

We can draw a qualitative pressure-volume diagram for such a parcel (see Fig. 4) using the facts stated above. During each closed cycle the parcel performs net work which is delivered to the surrounding gas. The parcel also transfers an amount of heat, receiving it from warmer part of the wall and delivering it to the colder part of the wall. Imagine a line of such neighboring parcels stretching along the hole in the plastic part from one end to the other. Together they transfer the same amount of heat from the hot end to the cold end of the plastic part during each thermodynamic cycle. The transfer of heat by neighboring parcels takes place as a bucket

brigade. At the same time, each one of the parcels delivers net work, which is manifested as a contribution to the acoustic power of the standing wave in the oscillator.

As we have shown, the thermoacoustic engine is a heat engine since it converts part of the heat that flows from the high temperature heat source to the low temperature heat sink into acoustic energy. The two copper disks soldered to the copper tubes act as heat source and heat sink. That is why they are called "heat exchangers."

Let us stress two important conditions. First, the gas parcel and the wall must be in imperfect thermal contact. Second, a large enough temperature gradient must be provided in the plastic part. If the gas parcel were touching the wall (if the thermal contact were perfect), the temperature of the parcel would be equal to the temperature of the adjacent wall at every point of displacement. While moving left the parcel would pass through exactly the same thermodynamic states as while moving right. The area of the cycle in the pressure-volume diagram would therefore be zero. Similarly, no net work would be done by a parcel far away from the wall (no thermal contact with the wall)—the thermodynamic states of such a parcel would be confined to a single adiabat (dotted line in Fig. 3). Concerning the second condition: what would happen if the temperature gradient in the plastic part were smaller? The amount of exchanged heat would decrease and, consequently, the pressure-volume diagram of the parcel would flatten (dotted curve in Fig. 4). The work done by the parcel would decrease. Finally, if the gradient were small enough to equal the adiabatic temperature change of the parcel divided by its displacement amplitude, no heat would be exchanged and the pressure-volume diagram would be reduced to a single adiabat.

Similar thermoacoustic engines have been presented before. Swift¹ used a propane flame to deliver heat to the hot part of the engine and room-temperature water to absorb the heat rejected in the cold part. Wheatley *et al.*² presented a thermoacoustic oscillator that was cooled with liquid nitrogen and kept warm with the hand on the other side. Both engines were made of copper tubes and with similar internal geometry—a stack of thin stainless steel plates (0.08 mm thick, 0.4 mm spacing) or plastic plates (0.38 mm thick, 1 mm spacing), with a stack of similar copper fins (heat exchangers) on each side.

We tried to keep the construction of the thermoacoustic engine as simple as possible. To achieve a suitable temperature gradient we choose cooling with liquid nitrogen so the copper parts could simply be soft-soldered. We avoided the complicated construction and alignment of three stacks by introducing the "sandwich" of a thick plastic disk between two thin copper disks. More than 200 holes (each 1.5 mm diameter) were drilled through the sandwich to provide a large active area open to gas flow.

This simplified engine consists of three mechanically robust and easily separated parts. This enables the demonstrator to disassemble the engine before the demonstration and hand the parts to the audience for a hands-on inspection of the simplicity of the thermoacoustic engine and to show that there are no moving parts inside. For the demonstration all we need are a thermoacoustic engine, a small Dewar vessel with an appropriately wide opening, one liter of liquid nitrogen, and tools for disassembling and assembling the engine.

This work was partially supported by the Ministry of Education, Science and Sport, Republic of Slovenia.

^{a)}Electronic mail: andrejj@fiz.uni-lj.si

¹Gregory W. Swift, "Thermoacoustic engines," *J. Acoust. Soc. Am.* **84**, 1145–1180 (1988).

²J. Wheatley, T. Hofler, G. W. Swift, and A. Migliori, "Understanding some

simple phenomena in thermoacoustics with applications to acoustical heat engines," *Am. J. Phys.* **53**, 147–162 (1985).

³Gregory W. Swift, "Thermoacoustic engines and refrigerators," *Phys. Today* **22–28**, (1995).

Listening to the coefficient of restitution and the gravitational acceleration of a bouncing ball

C. E. Aguiar^{a)} and F. Laudaes^{b)}

Instituto de Física, Universidade Federal do Rio de Janeiro, Cx.P. 68528, Rio de Janeiro, 21945-970, RJ, Brazil

(Received 15 July 2002; accepted 4 October 2002)

We show that a well known method for measuring the coefficient of restitution of a bouncing ball can also be used to obtain the gravitational acceleration. © 2003 American Association of Physics Teachers. [DOI: 10.1119/1.1524166]

Three contributions to this journal have described how to measure the coefficient of restitution between a ball and a flat surface using the sound made by the collision of the ball with the surface.^{1–3} The procedure reported in these papers is to drop the ball vertically on a horizontal surface, allow it to bounce several times, while recording the sound produced by the impacts. Analysis of the recording gives the time intervals between successive rebounds, and from these the coefficient of restitution is obtained.

The evolution of the techniques described in these papers is a nice example of how the development of microcomputers has changed the science teaching laboratory. In 1977, Bernstein¹ detected the sound with a microphone, amplified and filtered the signal, and fed it to a pen recorder. Smith, Spencer, and Jones,² in 1981, connected the microphone to a microcomputer via a homemade data collection and interface circuit, and then uploaded the resulting data to a larger computer for analysis and graphical display. In 2001, Stensgaard and Lægsgaard³ used the microphone input of a PC sound card to make the recording, thus reducing the equipment requirements to a standard microcomputer.

To see how the coefficient of restitution ϵ is related to the time between bounces, note that if ϵ is constant (independent of velocity), and air resistance is negligible, the velocity of the ball just after the n th bounce on the fixed surface is given by

$$v_n = v_0 \epsilon^n, \quad (1)$$

where v_0 is the velocity just before the first impact. The time-of-flight T_n between the n th and $(n+1)$ th collisions is proportional to v_n ,

$$T_n = \frac{2v_n}{g}, \quad n = 1, 2, \dots, \quad (2)$$

where g is the gravitational acceleration. Thus

$$T_n = T_0 \epsilon^n, \quad (3)$$

where we have defined $T_0 \equiv 2v_0/g$. Taking the logarithm of both sides of Eq. (3) we obtain

$$\log T_n = n \log \epsilon + \log T_0, \quad (4)$$

so that the plot of $\log T_n$ vs n is a straight line of slope $\log \epsilon$ and intercept $\log T_0$. Thus, as long as it is independent of

velocity, the coefficient of restitution can be obtained by fitting the straight line of Eq. (4) to the time-of-flight data.

The purpose of this note is to point out that this straight-line fit can also be used to determine another physical quantity of interest: the gravitational acceleration g . The (rather simple) observation is that, if the ball is released from a known height h , then $T_0 = (8h/g)^{1/2}$, and

$$g = \frac{8h}{T_0^2}. \quad (5)$$

Thus, just as the slope parameter of Eq. (4) fixes the coefficient of restitution, the intercept parameter determines the acceleration of gravity (if the easily measured initial height h is known).

In order to check how this works in practice, we have dropped a "superball" from a measured height onto a smooth stone surface and recorded the sound produced by the successive impacts. The recording was made with the microphone and sound card of a personal computer running Windows, using the sound recorder program that comes with the operating system. The sampling frequency was 22 050 Hz, resulting in a time resolution of 45 μ s. The audio file, stored in the binary WAV format, was converted to ASCII text format with the shareware program AWAVE AUDIO.⁴ The recorded signal is plotted in Fig. 1, where the pulses corre-

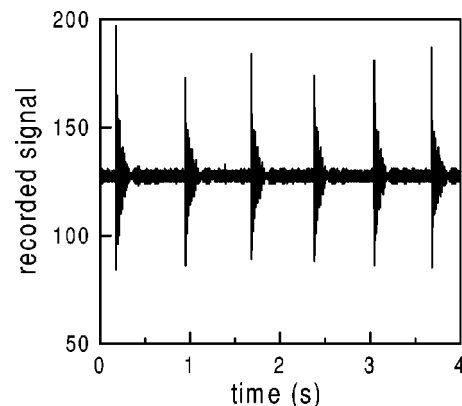


Fig. 1. The sound of a ball bouncing on a horizontal surface. The zero sound level corresponds to 128 on the vertical axis.

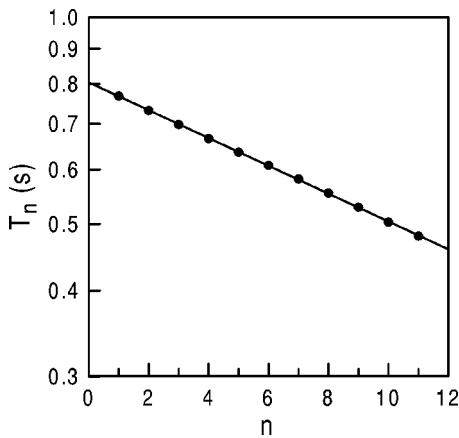


Fig. 2. Time-of-flight T_n between impacts n and $n+1$. The line is the least-squares fit using Eq. (4).

sponding to individual impacts are easily recognized (only the first six collisions are shown). We have used 8-bit resolution in the recording, so that data values can only go from 0 to 255. The no-signal value corresponds to 128.

The time intervals T_n between collisions n and $n+1$ were obtained directly through inspection of the ASCII sound file. They are plotted in Fig. 2 (in logarithmic scale) as a function of n . The least-squares fit of the T_n data set to Eq. (4) gives

$$\epsilon = 0.9544 \pm 0.0002, \quad (6a)$$

$$T_0 = 0.804 \pm 0.001 \text{ s}. \quad (6b)$$

The best-fit line is also shown in Fig. 2.

The ball was released from a height $h = 79.4 \pm 0.1$ cm above the surface. Taking this and the adjusted T_0 into Eq. (5), we obtain for the gravitational acceleration

$$g = 982 \pm 3 \text{ cm/s}^2.$$

For comparison, the value of g in Rio de Janeiro is 978.8 cm/s^2 .

The applicability of the method described above depends on ϵ being constant over the range of impact velocities involved in the experiment. That this condition is satisfied in the present case is seen in Fig. 3, where the coefficient of restitution for an impact at velocity v_n , $\epsilon = v_{n+1}/v_n$

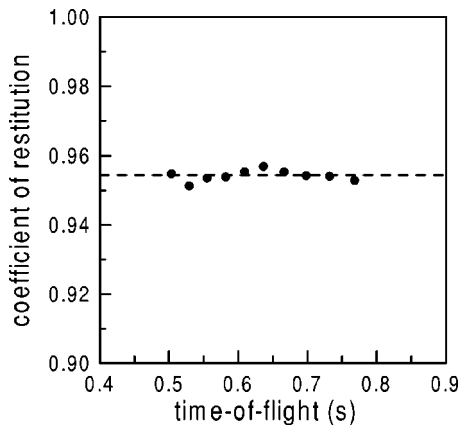


Fig. 3. The coefficient of restitution $\epsilon = T_{n+1}/T_n$ as a function of the time-of-flight T_n , for the data of Fig. 2. The dashed line indicates the adjusted value given in Eq. (6).

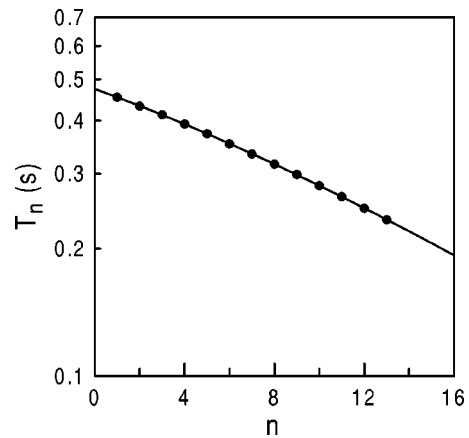


Fig. 4. Time-of-flight T_n between impacts n and $n+1$. The curve is the least-squares fit using Eq. (8).

$= T_{n+1}/T_n$, is plotted as a function of T_n [recall that $v_n \propto T_n$, see Eq. (2)]. The coefficients of restitution for the different impacts are all very close to the least-squares value given in Eq. (6), indicated by the dashed line in Fig. 3.

A case in which the coefficient of restitution depends on the velocity is shown in Fig. 4, where we display the times of flight of a superball dropped from $h = 27.5 \pm 0.1$ cm onto a wood surface. A plot of ϵ at each collision, shown in Fig. 5, reveals a clear dependence of the coefficient of restitution on the time-of-flight (or impact velocity). Assuming a linear relation between ϵ and T , as suggested by Fig. 5,

$$\epsilon = \epsilon_0(1 + \alpha T), \quad (7)$$

we obtain an extension of Eq. (3),

$$T_n = T_0 \epsilon_0^n \prod_{i=0}^{n-1} (1 + \alpha T_i). \quad (8)$$

The least-squares fit of Eq. (8) to the data shown in Fig. 4 gives

$$\epsilon_0 = 0.921 \pm 0.001, \quad (9a)$$

$$\alpha = 0.078 \pm 0.003 \text{ s}^{-1}, \quad (9b)$$

$$T_0 = 0.4752 \pm 0.0005 \text{ s}. \quad (9c)$$

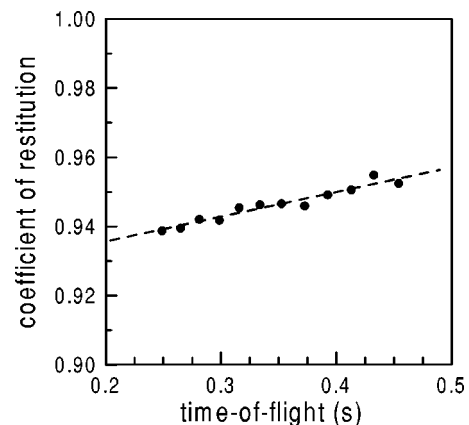


Fig. 5. The coefficient of restitution $\epsilon = T_{n+1}/T_n$ as a function of T_n , for the data of Fig. 4. The dashed line is the linear relation of Eq. (7) with the adjusted parameters given in Eq. (9).

The curves corresponding to these parameters are also shown in Figs. 4 and 5. The above value for T_0 yields

$$g = 974 \pm 5 \text{ cm/s}^2,$$

again a very reasonable value. Consideration of the velocity dependence of the coefficient of restitution was important in order to get an accurate result; had we assumed a constant ϵ , we would obtain $g = 935 \pm 10 \text{ cm/s}^2$.

To summarize, we have seen that the value of the gravitational acceleration is a useful by-product of experiments devised to “hear” the coefficient of restitution of a bouncing ball. The measurement of g is particularly simple if the coefficient of restitution is independent of the impact velocity, but more complicated cases can also be handled.

After this work was completed we learned of a recent paper by Cavalcante *et al.*,⁵ in which g was measured using the sound of a bouncing ball. The analysis presented in the

paper is, however, somewhat different from ours. Another related reference is the paper by Guercio and Zanetti⁶ in this journal.

^{a)}Electronic mail: carlos@if.ufrj.br

^{b)}Electronic mail: f_launders@hotmail.com

¹A.D. Bernstein, “Listening to the coefficient of restitution,” *Am. J. Phys.* **45**, 41–44 (1977).

²P.A. Smith, C.D. Spencer, and D.E. Jones, “Microcomputer listens to the coefficient of restitution,” *Am. J. Phys.* **49**, 136–140 (1981).

³I. Stensgaard and E. Lægsgaard, “Listening to the coefficient of restitution—revisited,” *Am. J. Phys.* **69**, 301–305 (2001).

⁴AwaveAudio (audio file format converter), FMJ-Software, <http://www.fmjsoft.com>

⁵M.A. Cavalcante, E. Silva, R. Prado, and R. Haag, “O estudo de colisões através do som,” *Revista Brasileira de Ensino de Física* **24**, 150–157 (2002).

⁶G. Guercio and V. Zanetti, “Determination of gravitational acceleration using a rubber ball,” *Am. J. Phys.* **55**, 59–63 (1987).

Automation of the Franck–Hertz experiment and the Tel-X-Ometer x-ray machine using LABVIEW

W. Fedak,^{a)} D. Bord, C. Smith, D. Gawrych, and K. Lindeman

Department of Natural Sciences, University of Michigan–Dearborn, Dearborn, Michigan 48128

(Received 10 June 2002; accepted 17 October 2002)

We describe the use of LABVIEW to automate data collection and instrument control for the Franck–Hertz experiment and for the popular Tel-X-Ometer x-ray machine. Such automation permits the rapid collection and reduction of large amounts of data, thus facilitating exploration of the basic physics of these experiments. The use of industry-standard software packages, such as ORIGIN and MATHEMATICA, provides students with valuable exposure to professional tools for the display and analysis of data. © 2003 American Association of Physics Teachers.
[DOI: 10.1119/1.1527949]

I. INTRODUCTION

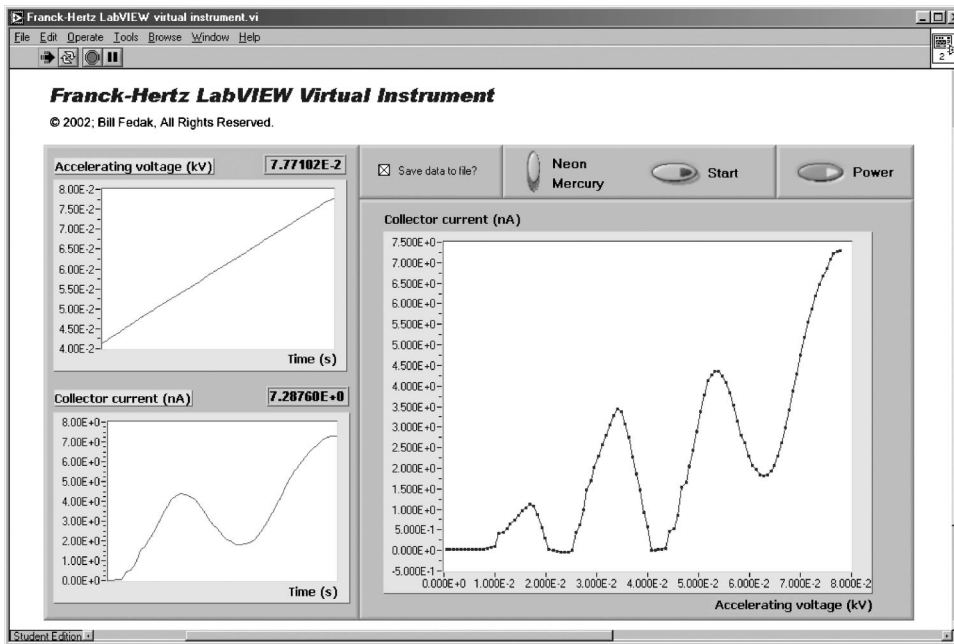
In this paper we describe the use of LABVIEW,¹ an industry-standard software package for data acquisition and instrument control, to automate the Franck–Hertz (FH) experiment and the Tel-X-Ometer^{2,3} x-ray machine. The FH experiment is a standard advanced undergraduate laboratory activity that demonstrates the existence of quantized energy levels in atoms. The Tel-X-Ometer x-ray machine is a popular laboratory device for investigating a wide variety of phenomena associated with the production, absorption, and scattering of x-rays.^{4,5} The automation of these experiments can reduce significantly the amount of time spent by a student performing routine data collection, as well as provide digitized formats that lend themselves to easy display, analysis, and comparison of data. Together, these enhancements of the experiments enable students to focus more directly on the physics of the investigation.

LABVIEW facilitates the development of graphical programs appropriately called *virtual instruments* (VIs). The user interface of a LABVIEW program resembles the front panel of a real laboratory instrument with dials, push buttons, toggles, and various digital and analog readouts. The program logic is created graphically by building block diagrams that consist of objects (functions and controls) and wires that transfer data between objects.

LABVIEW instrument drivers are available for hundreds of

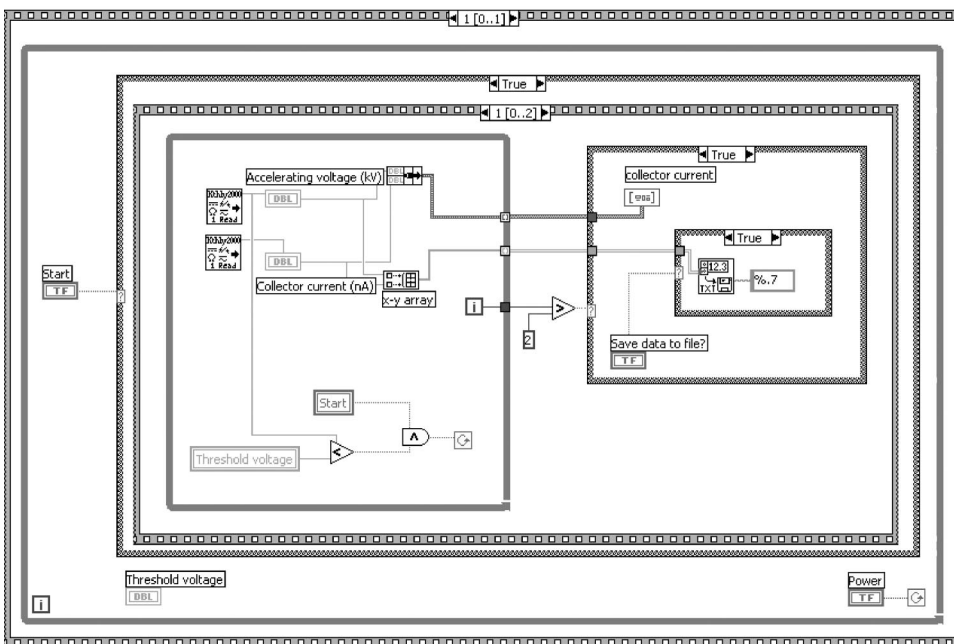
different data acquisition devices, allowing wide use of existing laboratory equipment.⁶ LABVIEW versions are available for Microsoft Windows, Apple Macintosh, Sun Solaris, HP-UX, and Linux operating systems.⁷ Given the increasingly common use of LABVIEW in college and university electronics courses, many students may already be familiar with the software.⁸ For example, our instrumentation course, which is a prerequisite for the advanced lab course, now includes basic LABVIEW programming.

We have written LABVIEW VIs for both the FH experiment and for the Tel-X-Ometer x-ray machine. The FH VI provides fast and accurate data collection, as well as real-time display of the FH curves. The Tel-X-Ometer VI provides precise instrument control and automated data collection. The acquired data in both cases can be saved to a text-delimited file, permitting detailed data analysis and display using software packages such as ORIGIN⁹ and MATHEMATICA.¹⁰ Although LABVIEW routines can be written to analyze the acquired data and calculate various results (for example, the mean FH peak separation or the $\text{Cu } K_\alpha$ wavelength), we intentionally left the data analysis portion out of our LABVIEW VIs to avoid making each experiment a “black box.” Data analysis software such as ORIGIN and MATHEMATICA is ideally suited to such analysis and provides valuable “real-world” experience using professional software tools. Students with LABVIEW programming expertise are



(a)

Fig. 1. (a) LABVIEW virtual-instrument front panel for the Franck-Hertz experiment showing data collected during one run with the Ne tube, and (b) block diagram (program code).



(b)

encouraged to modify the VIs. The ability to write and modify LABVIEW programs has been found to be a marketable skill for physics students entering the high-technology workplace.^{8,11}

II. FRANCK-HERTZ EXPERIMENT

Automation of the FH experiment has been a frequent subject of discussion in this journal. Adelberger and Kinsey¹² have described the use of an oscilloscope, as suggested by Melissinos,¹³ to provide a real-time display of the characteristic FH curves (accelerating voltage versus collector current). In this method, a camera is used to photograph the oscilloscope display, thus providing a permanent record of the curves. The spacing between the peaks of the curves can

be measured directly from the oscilloscope display or from the photograph. Carpenter¹⁴ has described the use of an $x-y$ recorder as an output device to plot the curves. Such plots provide greater resolution than oscilloscope photographs and at less cost. Nornes and Tu¹⁵ have suggested further automation of the experiment using a BASIC program running on a computer that is coupled to the FH equipment via an IEEE-488 interface. Such a setup provides a real-time display of the acquired data that can be sent to a printer. BASIC programs can be written to locate the peak positions and determine their separations.

A. FH experimental setup and LABVIEW VI

Our experimental setup consisted of the following Leybold equipment: a FH supply unit (No. 555 88), an electric

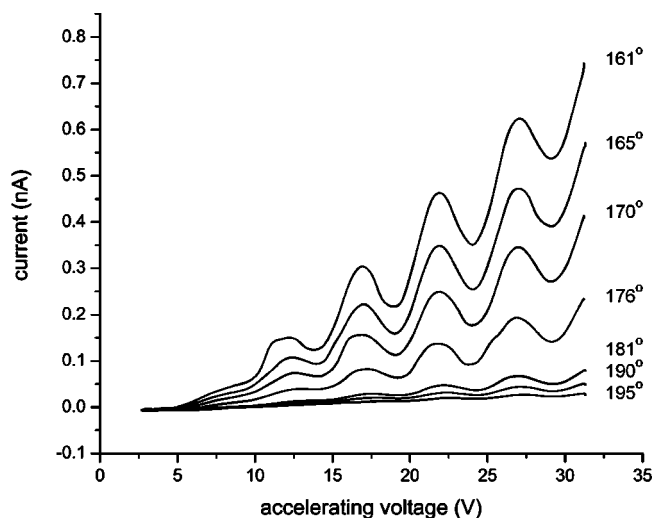


Fig. 2. Plot of accelerating voltage vs collector current for various Hg tube temperatures in units of degrees celsius.

oven, a Hg tube and connection socket, a Ne tube and holder (No. 555 871), and a temperature sensor. The accelerating voltage and collector current outputs of the supply unit were connected to a pair of Keithley 2000 digital multimeters.¹⁶ These in turn were connected through a GPIB bus to a National Instruments PCI-GPIB interface board installed in a standard Intel Pentium II-based IBM-compatible computer. The accelerating voltage is controlled by the FH supply unit and can be set to ramp automatically from 0 to 30 V for the Hg tube or from 0 to 80 V for the Ne tube. The accelerating voltage can also be controlled manually within these voltage ranges. The temperature of the Hg tube can be set using the supply unit; the Ne tube operates at room temperature.

LABVIEW (version 6.0) was used to create a VI to read the accelerating voltage and collector current values simultaneously from the Keithley digital multimeters. The accelerating voltage versus collector current is displayed in real-time, building-up the characteristic FH curve as data are

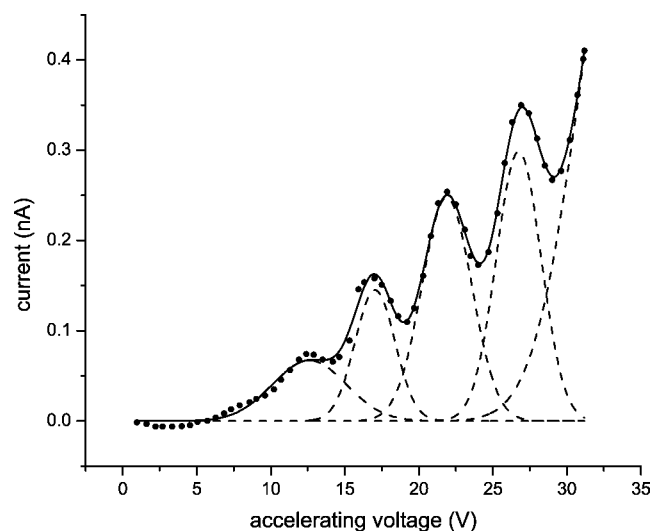


Fig. 3. Multiple Gaussian functions (dashed lines) are fitted to the characteristic Franck-Hertz data (closed circles) for Hg using the ORIGIN software. The resulting composite function (solid line) can be analyzed using MATHEMATICA to determine the peak positions precisely.

collected. Figures 1(a) and 1(b) show the front panel and the block diagram, respectively, of our FH VI. The tube type can be set to either Ne or Hg. The user is given the option of saving the data to a file. The VI has been programmed to collect data until a threshold accelerating voltage has been reached, allowing either automatic or manual ramping of the accelerating voltage. High-resolution curves can be acquired by manually ramping the accelerating voltage very slowly. Different data acquisition hardware may be accommodated by replacing the two Keithley drivers with ones appropriate to the devices available in the user's lab. The only modification we made to the standard Keithley driver¹⁶ was to set the IEEE hardware addresses.

B. Application

We have used this experimental setup to examine the effect of varying the Hg tube temperature on the shape of the FH curve. As the temperature is increased, it is expected that an electron is more likely to undergo a collision while passing through the Hg vapor (the mean free path for the electrons will be shorter), thus lowering the collector current.^{13,17} We ran the experiment for various temperature settings and saved the collected data in a series of files. We then imported these data sets into ORIGIN to create the plot shown in Fig. 2. The process of acquiring, importing, and plotting this data took less than 20 min, with most of the time spent waiting for the oven temperature to change.

It is immediately evident from the plot that the collector current generally decreases with increasing temperature. The spacing of the peaks is not appreciably affected over this temperature range, although the peak amplitudes are greatly reduced. To determine the peak spacing, we first used ORIGIN to fit multiple Gaussian functions to the characteristic FH curves, as shown in Fig. 3. The center of each Gaussian function corresponds closely with each peak location. We then used MATHEMATICA to determine the maxima of the peaks by finding the zeros of the derivative of the fitted function. For the 170 °C data shown in Fig. 3, the mean peak spacing was 4.86 ± 0.34 eV, in good agreement with what is expected from a careful analysis of the known Hg energy levels.¹⁸

Other possible student investigations include examining the effect of changing the grid voltages on the FH curves, and monitoring collector current fluctuations at specific grid voltage and temperature settings.

III. TEL-X-OMETER X-RAY MACHINE

Over 15 years ago in this journal, Barry and Brothers described the interfacing of the Tel-X-Ometer with a computer to automate data collection.¹⁹ In their setup a metal shaft was machined to replace the plastic thumbwheel shaft. A potentiometer connected to the metal shaft was used in a voltage divider circuit that was sampled by an analog-to-digital converter, thus providing digital values of the angular position of the slide carriage arm. X-ray events were counted using a simple counting circuit and a short machine language timing program. The acquired data (counts per angle) were recorded to a text-file for later plotting and analysis. The movement of the slide carriage arm was not automated; it had to be moved into position manually for each angle at which data was to be collected.

In the early 1990s, TEL-Atomic Incorporated, the U.S. distributor of the Tel-X-Ometer, offered an optional automa-

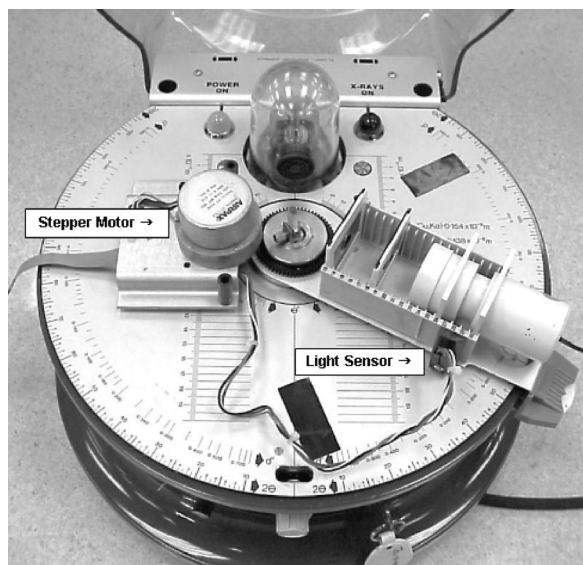


Fig. 4. Tel-X-Ometer and stepper motor assembly.

tion kit consisting of a stepper motor, a stepper motor controller, a drive gear assembly, a light sensor, a mounting assembly, and DOS-based data acquisition and analysis software. The light sensor is installed on the slide carriage arm of the Tel-X-Ometer and is used to establish the end points of the arm's travel by detecting nonreflective tape strips affixed to the surface of the Tel-X-Ometer. Figure 4 shows the Tel-X-Ometer with the stepper motor and light sensor installed. This equipment has the advantage of allowing data acquisition and instrument control using the standard printer port on a computer; no special data acquisition control boards are required. The software was written for IBM 8088/286 computers and was last updated in 1991. Unfortunately, the signals used to control the stepper motor were timed with processor cycles rather than with the inter-

nal clock pulses of the computer system. Modern computers run software at such high speed that the stepper motor will not respond to the control pulses.²⁰

Although this automation kit is no longer available from TEL-Atomic, they now offer an auto-scanning kit (TEL 2003/2030) that includes a scan console control unit, a stepper motor, and a mounting bracket. This kit can be interfaced with a ratemeter or data logger to count events, but does not include software or an interface for computer-based instrument control and data acquisition.

A. LABVIEW virtual instrument

Our LABVIEW VI was written to work with the original TEL-Atomic automation kit hardware and to replace the old DOS-based software. Figure 5 shows the front panel (user interface) of this VI. The front panel includes: (1) controls to rotate the slide carriage, (2) indicators to show the current angle and event triggers, (3) a calibration routine to set the number of steps per degree, (4) settings for automated data acquisition, and (5) a display of the acquired data. The delay between stepper motor steps can also be adjusted; our stepper motor required a minimum delay of 15 ms. Shorter delays resulted in signal pulses with a repetition period less than the stepper motor response time, hence causing missed steps and loss of calibration. For automated data acquisition, the system sweeps through a preset angle at a given step resolution and counts events at each of the intermediate angles for a preset number of seconds. The step resolution determines the number of steps between each intermediate angle at which data are collected; it can be set anywhere in the range from 1 step to 16 steps.

B. Application

To illustrate the power and simplicity of our automated setup, we have used it to determine the wavelengths of the K_{α} and K_{β} peaks for Cu. In addition to the Tel-X-Ometer

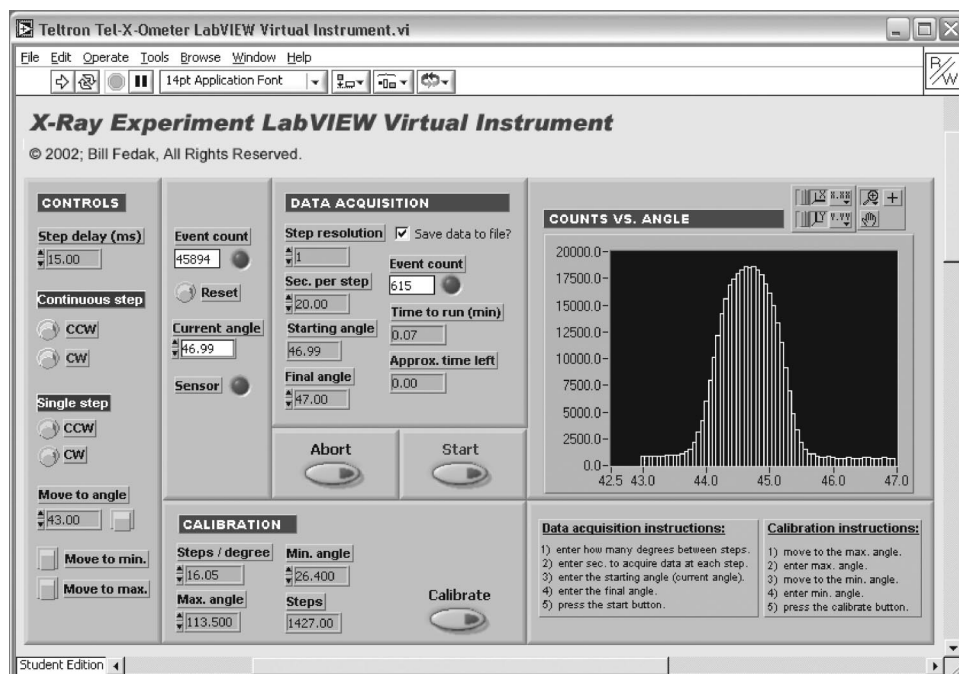


Fig. 5. LABVIEW virtual instrument front panel for the Tel-X-Ometer x-ray machine.

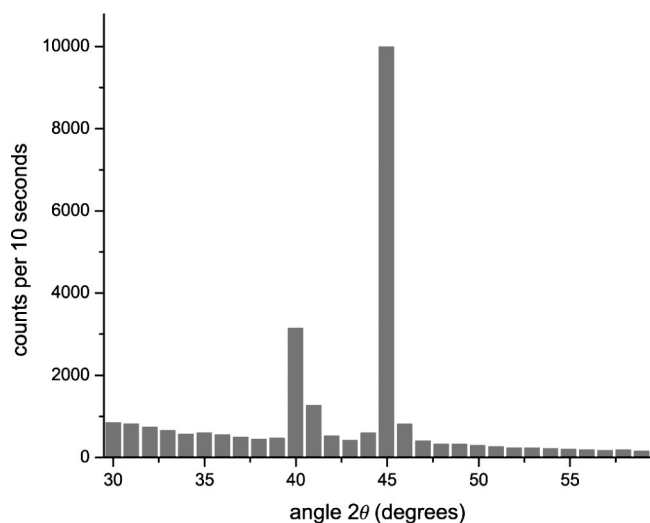


Fig. 6. First-pass, low-resolution plot of counts per angle showing the approximate locations of the K_{α} and K_{β} peaks for Cu. The run-time to collect the data for this plot was only 5 min.

580M x-ray machine and Geiger-Muller (GM) tube, a Keithley 485 auto-ranging picoammeter was used to monitor the current in the x-ray tube and a Nucleus Model 575 Scaler-ratemeter was used to count x-ray events. We modified our Nucleus ratemeter to provide 0–5 V pulses, through its internal speaker circuit, to the Tel-Atomic stepper motor controller. A LiF crystal with lattice spacing $d=0.2015$ nm was used as an x-ray diffraction grating. To determine the wavelengths of the K_{α} and K_{β} peaks we invoked Bragg's Law, $n\lambda = 2d \sin\theta$ where n is the order of diffraction and θ is the angle of incidence as measured from the face of the crystal. Note that the angles imprinted on the face of the Tel-X-Ometer and referred to in our LABVIEW VI are the 2θ angular measure customarily used in x-ray diffraction.

The combination of LABVIEW and the Microsoft Windows environment results in high computing “overhead,” thus limiting how fast the parallel port can be polled to count events. An AMD Athlon-based computer system with a 1.2-GHz processor was used to run the LABVIEW application. It supports count rates in excess of 60 000 per minute, which is more than adequate to handle the limiting count rate for GM tubes with dead times that are typically 0.1 ms. Higher count rates could be accommodated by using a higher performance computer or by using a data acquisition board to interface directly to the ratemeter instead of acquiring data through the parallel port.

In the typical manual mode of operation, the slide carriage is moved by hand and counts are acquired for some preset time at each angle. When performed in this fashion, the maximum angular resolution is approximately 10 arcmin. Our automated setup increases this resolution to 3.75 arcmin (16 steps per degree). Large numbers of counts per angle can be collected conveniently, thus increasing the precision of the results.

We first performed a low-resolution first-pass scan by setting the starting angle to 30° , the final angle to 60° , the step resolution to 16 steps (1° angular resolution), and the count time to 10 s per step. The run-time to collect the data was only 5 min. Both the K_{α} and K_{β} peaks were readily apparent in the resulting plot shown in Fig. 6, with the first-order K_{α} peak appearing at approximately 45° and the first-order K_{β}

peak near 40° . The rough location of peaks can be found quickly in this way, which is helpful in eliminating any setup, calibration, or alignment errors prior to running a lengthy high-resolution scan.

We next performed a high-resolution scan between 43° and 46° to determine the precise location of the K_{α} peak. The step resolution was set at 1 step ($\frac{1}{16}^{\circ}$) and the count time at 20 s per step, resulting in an experimental run-time of 16 min. The maximum count rate was under 1000 events per s. The text-file of acquired data was imported into ORIGIN and the K_{α} peak was located at $44.81 \pm 0.25^{\circ}$. The K_{β} peak position was determined to be $40.11 \pm 0.25^{\circ}$ by scanning from 39° to 41° using the same resolution settings. The resulting x-ray wavelengths are $\lambda_{\alpha} = 0.1536 \pm 0.0008$ nm and $\lambda_{\beta} = 0.1389 \pm 0.0008$ nm, in good agreement with tabulated values.²¹ These wavelengths can subsequently be used to determine the atomic spacing for other crystals such as NaCl.

IV. CONCLUSION

We have found many advantages to using LABVIEW to automate experiments and to using software such as ORIGIN and MATHEMATICA to simplify data analysis. The simplification of the task of data collection greatly increases student productivity. Time that is typically spent doing routine data collection can instead be used to explore the physics of the experiments and to perform a greater number of experiments. Students gain valuable experience using research-grade instrument control, data acquisition, and data analysis software, which can prove useful in future scientific or industrial research. Because the experimental data are obtained in an electronic format, students can receive immediate feedback by analyzing the data during an experiment, which can be useful in correcting errors in alignment, configuration, or setup, as well as suggest areas of further investigation. The precision of the data is often increased significantly using an automated setup.

We found LABVIEW VIs to be simple to create, modify, and extend. The wide availability of LABVIEW instrument drivers permits the use of existing, on-hand data acquisition hardware. It is worth noting that LABVIEW can be used to develop web-enabled VIs for remote access to laboratory equipment, thus permitting real-time data collection over the internet.²²

ACKNOWLEDGMENTS

We would like to thank Dr. Alfons Schute of the Department of Physics, University of Central Florida, for providing an initial example of a LABVIEW VI utilizing the Keithley instrument driver. Thanks are also due to Dr. Paul Zitzewitz for his review of an early draft of this manuscript.

^{a)}Electronic mail: bfedak@umd.umich.edu

¹National Instruments Corporation, 11500 N. Mopac Expressway, Austin, TX 78759; www.ni.com.

²TEL-Atomic Incorporated, P.O. Box 924, Jackson, MI 49204; www.tel-atomic.com.

³T. H. Zepf, “The Tel-X-Ometer—An Evaluation,” *Phys. Teach.* **17** (5), 330–333 (1979).

⁴R. D. Piccard and S. A. Carter, “Using nonexponential absorption to demonstrate that anode x rays are polychromatic,” *Am. J. Phys.* **57** (10), 931–936 (1989).

⁵P. Russo and A. D. Brothers, “Powder diffraction patterns on the Tel-X-Ometer 80,” *Am. J. Phys.* **50** (1), 89–90 (1982).

- ⁶LABVIEW device drivers can be found at the National Instruments website: www.ni.com.
- ⁷J. Essick, *Advanced LabVIEW Labs* (Prentice Hall, Upper Saddle River, NJ, 1999).
- ⁸J. A. Panitz, "Contemporary electronics: A focussed concept laboratory," *Am. J. Phys.* **70** (3), 280–284 (2002).
- ⁹OriginLab Corporation, One Roundhouse Plaza, Northampton, MA 01060; www.originlab.com.
- ¹⁰Wolfram Research, Inc., 100 Trade Center Drive, Champaign, IL 61820; www.wolfram.com.
- ¹¹T. D. Usher and P. K. Dixon, "Physics goes practical," *Am. J. Phys.* **70** (1), 30–36 (2002).
- ¹²R. E. Adelberger and K. F. Kinsey, "An Automated Franck–Hertz Experiment," *Am. J. Phys.* **40** (2), 349–350 (1972).
- ¹³A. Melissinos, *Experiments in Modern Physics* (Academic, New York, 1966), pp. 8–17.
- ¹⁴K. H. Carpenter, "An automated Franck–Hertz experiment using an X-Y recorder," *Am. J. Phys.* **43** (2), 190–191 (1975).
- ¹⁵S. Normes and Y. Z. Tu, "Augmenting traditional undergraduate advanced laboratory experiments by automation using IEEE-488 and RS-232 interfaces," *Am. J. Phys.* **57**(10), 937–940 (1989).
- ¹⁶Keithley Instruments, Inc., 28775 Aurora Road, Cleveland, OH 44139; www.keithley.com.
- ¹⁷F. Reif, *Fundamentals of Statistical and Thermal Physics* (McGraw–Hill, New York, 1965), pp. 469–470.
- ¹⁸G. F. Hanne, "What really happens in the Franck–Hertz experiment with mercury?," *Am. J. Phys.* **56** (8), 696–700 (1988).
- ¹⁹P. J. Barry and A. D. Brothers, "Interfacing a Tel-X-Ometer with a micro-computer," *Am. J. Phys.* **54** (2), 186–187 (1986).
- ²⁰We originally used the program "MO'SLO" to slow down the execution of the DOS program to 1% of normal speed. We were then able to run the program but still encountered difficulties in collecting data accurately. MO'SLO is available from Hearn/Perrell Art Associates, 23022 Hatteras Street, Woodland Hills, CA 91367; www.hpaa.com.
- ²¹*Handbook of Physics*, edited by W. Benenson, J. W. Harris, H. Stocker, and H. Lutz (Springer, New York, 2002), p. 1086.
- ²²P. A. Tompkins and G. Pinggen, "Real-Time Experimentation Across the Internet," *Phys. Teach.* **40** (7), 408–410 (2002).